Engineering Research Journal
journal homepage: https://erj.journals.ekb.eg/

Enhancing the Overall Performance of High-Concentration Photovoltaic/Thermal Systems Employing Hybrid Cooling Topologies

Ahmed M. I. Abutalib[a,*], Mostafa M. Abd El-Samie[a,b *], M. A. M. Hassan[a]
[a]Laboratory of Thermodynamics, Faculty of Engineering (Elmataria), Helwan University, Cairo, Egypt.
[b] Mechanical and Nuclear Engineering Department, Khalifa University, Abu Dhabi, UAE.
[*]Corresponding author E-mail: ahmedibrahim777@m-eng.helwan.edu.eg

Abstract

High-concentrated photovoltaic (PV) panels encounter critical challenges, such as the non-uniform distribution of the solar spectrum and diminished efficiency, which significantly impact their overall performance and long-term durability. This study presents a novel hybrid cooling topology, which combines a spider network as a heat sink with jet impingement technology. This cooling topology employs a hexagonal spider network of microchannels, featuring several jets and four outlet manifolds, designed to ensure optimal temperature uniformity across the PV panel. A series of multiphysics simulation activities is conducted to ensure accurate modeling of the optical, thermal, and electrical performance, integrating computational fluid dynamics (CFD) for thermal-electric analysis and Mote Carlo ray-tracing techniques for optical modeling. The reliability of the simulations is measured and verified. The overall performance of the concentrator photovoltaic/thermal (CPV/T) system is evaluated under different solar intensities (400-1200 W/m^2), coolant flow rates (0.5-1.3 kg/s), and manifold angles ($1-5^{\circ}$). The findings reveal that the lowest pumping power is achieved by a manifold angle of 5°. Moreover, the five-degree, four-outlet manifold design achieves superior performance with a total exergy efficiency of 9.28% and electrical energy efficiency of 8.96% at a flow rate of 1.3 kg/s. Compared to the previous design in the literature, the advanced cooling system enhances net electric power by 84.71%, net output power by 135.25%, reduces pumping power by 71.67%, and lowers temperature nonuniformity by 52.89%.

Keywords: High-concentration photovoltaic/thermal systems, hybrid cooling topology, energy and exergy analysis, net output power.

DOI: 10.21608/erj.2025.342458.1157
Received 07 December 2024; Received in revised form 25 January 2025; Accepted 29 January 2025
Available online 01 March 2025

Nomenclatures

A_{cell}	Surface area GaAs cell (m^2)
C_p	Specific heat capacity ($J\ kg^{-1}K^{-1}$)
CR	Solar concentration ratio (–)
E_g	Bandgap energy of PV cells (eV)
EQE	Solar cell external quantum efficiency (%)
$F(\lambda)$	AM1.5D spectral irradiance ($W\ m^{-2}\ nm^{-1}$)
FF	Fill factor of GaAs cell (–)
h_w	Water heat transfer coefficient ($W\ m^{-2}\ K^{-1}$)
I_{sun}	Total incident solar radiation ($W\ m^{-2}$)
J_{SC}	Short circuit current density ($A\ m^{-2}$)
J_{00}	Dark saturation current density ($A\ m^{-2}$)
k	Thermal conductivity ($W\ m^{-1}\ K^{-1}$)
k_B	Boltzmann's constant ($1.38066e^{-23}\ J\ K^{-1}$)
$\dot{m}$	Mass flow rate ($kg\ s^{-1}$)
n	Real refractive index (–)
P	Pixelation in control angles (–)
P_{th}	Absorbed thermal energy (W)
P_{ele}	Generated electric power (W)
q_{rad}	Rate of radiative heat transfer per unit volume ($W\ m^{-2}$) m^{-3}
$\vec{r}$	Direction vector (–)
S_h	Volumetric heat source ($W\ m^{-3}$)
$\vec{s}$	Position vector (–)
$\vec{s}'$	Scattering direction vector
T	Temperature (K)
V	Voltage (V)
V_{wind}	Wind speed ($m\ s^{-1}$)
$\vec{V}$	velocity vector (–)

Greek symbols

β	Scattering coefficient (m^{-1})
γ	Manifold angle (°)
δ	Temperature coefficient (K^{-1})
η	Energy efficiency (%)
η_{opt}	Optical efficiency of the system (%)
k	Absorbance rate (–)
k_λ	Absorption coefficient (m^{-1})
λ	Wavelength of photons (nm)
λ_g	Cutoff wavelength (nm)
μ	Dynamic viscosity ($Pa\ s$)
ξ	Exergy efficiency (%)
ρ	Density ($kg\ m^{-3}$)
σ	Extinction coefficient (m^{-1})
φ	Scattering phase function (–)
$\acute{\Omega}$	Solid angle (–)
∇	Operator (–)

Subscript

a	Ambient
b	black body
$cell$	GaAs cell
ele	Electric
f	Fluid
in	Flow inlet
OC	Open circuit
out	Flow outlet
PV	Photovoltaic
s	Solid
SC	Short circuit
t	Total
th	Thermal

Greek subscript

θ	Divisions in the azimuthal extent
λ	Certain wavelength
λ_g	Split at cutoff wavelength
ϕ	Divisions in the polar extent

Abbreviations

AM1.5D	Standard spectrum for terrestrial direct beam
CFD	Computational fluid dynamics
CPV	Concentrator photovoltaic
CPV/T	Concentrator photovoltaic/thermal system
DNI	Direct normal irradiance
DO	Discrete ordinates
FVM	Finite Volume Method
MCRT	Monte Carlo Ray-Tracing
MNSPHS	Modified net spider heat sink
PV/T	Photovoltaic/thermal
RTE	Radiative transfer equation
SR	Spectral response
UDF	User-defined function
WHR	Waste heat recovery

1- Introduction

The importance of developing renewable energy sources has grown in recent years due to rising environmental concerns and energy shortages. The most prominent and reliable renewable

energy source on our planet is solar power, which has recently attracted much attention. Photovoltaic (PV) and thermoelectric systems turn sunlight directly into electricity, while solar thermal systems utilize solar radiation to generate heat, which is then used to generate electricity [1]. When contrasted with more conventional methods of electricity generation, PV systems' high price tag and poor power conversion efficiency (PCE) stand out as significant drawbacks. By employing cost-effective concentrators such as parabolic troughs, dishes, or Fresnel lenses, high-concentrated photovoltaic (HCPV) systems mitigate these challenges by decreasing the quantity of costly semiconductor material required [2]. Monocrystalline, polycrystalline, and amorphous silicon cells exhibit decreasing PCEs of 0.45%, 0.45%, and 0.25% with each degree Celsius increase, respectively [3]. Temperature increases can lead to transient efficiency loss, localized overheating, and long-term damage, particularly in HCPV [4-6]. Improving CPV performance and eliminating hotspots and mismatches requires maintaining a consistent and low operating temperature using proper cooling systems [7].
Various passive cooling methods, such as heat pipes, phase change materials, and evaporation processes, were offered for CPV systems with concentration ratios (CRs) ≤ 20. On the other hand, a more powerful cooling system is needed to withstand the subsequent high temperatures in HCPV systems with higher CRs [8]. Various active cooling technologies are available for dissipating heat; some of the most well-known include microchannel heat sinks (MCHSs), forced air or liquid, jet impingement, and hybrid systems [9, 10].

Liquid cooling technology benefits MCHS systems because they may act as heat sinks or liquid cold plates when attached to HCPV and circuit surfaces. Large heat transfer area per volume and high heat transfer coefficient enables rapid heat transfer in MCHSs with sizes ranging from 10-200 μm or 1-4 mm. Several studies have investigated thermal performance and temperature uniformity in CPV schemes concerning the geometrical effects of MCHSs. Tuckerman et al. [11] found that the temperature profile grew more nonuniform as water ran through straight MCHSs, suggesting that the HCPV module needs improved thermal management. Lee et al. [12] replaced continuous fins with 26.6° oblique fins in MCHSs, disrupting the thermal boundary layer to improve heat transfer and temperature uniformity while slightly increasing the pressure drop near the outlet. According to Micheli et al. [13], the flat silicon wafer's maximum cell temperature was 78.8 ℃ under standard conditions. Nevertheless, the cell's temperature decreased substantially to 70.4 ℃ upon adding fins. Abo-Zahhad et al. [14] enhanced the cell temperature uniformity at a 1000 g/min flow rate by employing stepwise width modulation in microchannels, which improved HCPV performance while increasing pressure drop. Reddy et al. [15] found that high flow rates did not reduce the cooled surface temperature, even though microchannels that were 0.5 mm wide, 4 mm deep, and 12 mm long gave the lowest pressure drop.

In addition to factors like channel width, channel spacing, and inlet/outlet design [16], the cross-sectional geometry of the channels and other geometric characteristics of MCHSs are essential for improving their cooling Performance [17]. Due to secondary flow generation and flow variability within a preset optimal wave amplitude range, wavy MCHSs provide notable thermal performance advantages [18]. By increasing flow turbulence and disrupting hydraulic/thermal boundary layers, MCHSs with ribs and grooves can enhance heat transmission [19]. When comparing the double-layer MCHS to the single-layer MCHS, the structural optimization studies showed a modest increase in pressure drop and a decrease in heat resistance concerning the double-layer MCHS [20]. Yang et al. [21] suggested a multiple-layer MCHS system that effectively controls the cell's temperature, pressure drop, and nonuniform temperature. On the other hand, CPV systems were not as productive or economically viable when using MCHS alone because of their low heat transfer capacity, substantial pressure drop, and inconsistent temperature profile.

In addition, high local heat transfer coefficient applications and densely positioned PVs are both cooled by jet impingement in high-performance circuits. As a result, the heat transfer efficiency is restricted beyond the impingement zone due to the substantial temperature gradient observed [22]. Abo-Zahhad et al. [23] found that single jet bed configurations had the lowest cell temperature and most significant pressure drop, although numerous jet bed configurations provide cross-flow problems. An increase in the Nusselt number and a decrease in jet interaction with the wall were achieved at a maximum jet-to-jet distance four times the jet diameter [24]. However, as the jet impinged, the heat transfer coefficient outside the impingement region decreased, and temperature nonuniformity increased.

A cooling system that maximizes heat dissipation and temperature distribution has been achieved by combining jet impingement with MCHS [25]. A hybrid jet impingement-MCHS cooling system takes the best characteristics of both MCHSs and jet impingement and uses them in a hybrid design to create an extremely efficient cooling system. As a result of its exceptional heat-removal capabilities and ability to prevent hot patches, the cooling surface maintains a uniformly high temperature [26]. The use of hybrid jet impingement-MCHS systems to mitigate the operational temperatures of PV cells and resolve concerns regarding temperature nonuniformity has been extensively investigated in research. Abo-Zahhad et al. [27] also discovered that the peak temperatures and pressure drops are reduced when the specified dimensions of the MCHS along the fluid path are reduced. Hosny et al. [28] developed a less complicated and more effective system using a single or double microchannel section with jets. Torbatinezhad et al. [29] indicated that reducing the wavy mini-channel wavelength (the distance between two successive peaks of the wavy channel), raising jet angle, and augmenting coolant flow rate elevates cell temperature; nevertheless, this simultaneously raises pressure drop and fails to provide an effective solution for temperature nonuniformity.

Despite their advantages, the research highlights the limitations of jet impingement, MCHS, and hybrid jet impingement-MCHS systems. One issue is that less efficient cooling occurs over time because heat transfer efficiency decreases as fluid temperature increases in the direction of flow [27]. The second issue is that the flow is not evenly distributed since the coolants are not mixed enough between the channels [29]. The nonuniform temperatures caused by this poor distribution over the cell surface can adversely affect the system's performance and lifespan. Accordingly, additional research and innovation are necessary to overcome these limits and enhance the thermal management of these cooling systems.

Bionic topology, in which the flow pattern displays certain traits indicative of biology, has recently emerged as one of the most popular approaches to improving flow maldistribution. Spider webs, alveoli, honeycombs, leaf veins, and snowflakes are just a few examples of the bionic topologies that have inspired the creation of various crystal structures. Straight, ternate veiny, lateral veiny, snowflake-shaped, spider netted, and honeycomb MCHSs were the six varieties reviewed by Tan et al. [30]. It should be noted that hydraulic and thermal characteristics formed the basis of their investigation. Despite its more significant pressure drop, the results showed that spider-netted MCHSs had better thermal performance than straight, lateral, snowflake, ternate, honeycomb, and lateral MCHSs. Although bionic topologies are inventive in enhancing heat transfer and fluid distribution, their complex architecture and distinctive morphologies restrict design versatility. Its adaptability to different types and sizes of heat sources requires more development.

Based on the above literature, The current research introduces a novel hybrid jet impingement-microchannel system featuring a four-outlet manifold spider-netted configuration designed as a bionic topology to enhance cooling in HCPV applications, addressing existing deficiencies. Remember that problems with heat transfer along the flow direction and insufficient coolant cross-mixing between channels, leading to temperature inconsistencies and inadequate cooling,

are the targets of this strategy. It also seeks to simplify the system, shorten the cooling fluid path, and reduce pumping power requirements. Additionally, no investigation into such systems has focused on a nonuniform heat flux profile, which is applied here, indicative of the closeness to the actual operating conditions. In addition, there is a need to enhance thermal management because existing cooling methods have limitations such as high surface temperature, nonuniform temperature distribution, or high-pressure drop. So, from the point of view of ensuring reliable cooling solutions for HCPV systems, this study closes these knowledge gaps on a novel hybrid jet impingement MCHS with a spider-netted design. Consequently, the hydraulic, energy, and exergy performance characteristics of the HCPV system are evaluated by conducting a thorough analysis of the cooling scheme's design parameters using a complicated 3D CFD numerical model. The parameters to be investigated are the influence of DNI, manifold angle, and number of manifolds. Additionally, The spider-netted heat sink used in the literature (reference case) [30] is contrasted with the developed HCPV/T system, which features four-outlet manifolds at a fixed condition of 5° angle to evaluate the efficiency of the heat sink that has been developed.

2- Model description

Figure 1 shows a schematic of the HCPV/T solar system, which uses a parabolic dish to focus the Sun's rays on the receiver assembly. A rectangular dish is employed in the suggested model to achieve consistent illumination, which guarantees that the shape of the solar collector matches that of the highlighted area [7]. The absorber has a copper layer, a modified aluminum net spider for the heat sink, and GaAs solar cells (see section 3-2 for more information). Using GaAs solar cells, this process transforms solar energy into thermal energy and electricity. Adding a copper layer lets the GaAs cell and heat sink transport heat more efficiently. Hexagons with nested self-similarity on numerous layers form the microchannel with spider web netting attached to the backside of the copper layer to absorb the GaAs solar cell's excess heat. Spider webs can take many forms, including pentagons, decagons, and octagon polygons. The hexagon cooling configuration is applied according to a detailed comparing analysis of different microchannels topologies, provided by [30]. The water is used as a heat transfer fluid (HTF) passes through the hexagonal spider netted heat sink to maintain the solar cells' temperature at an appropriate level.

Most incoming radiation, particularly in the ultraviolet and mostly infrared, is transformed into heat. The rest is turned into electricity within the bandwidth of GaAs solar cells. According to Chemisana et al. [31], the PV-band spectrum bandwidth is determined by taking into account the spectral response (SR) of the GaAs cell as well as the solar characteristics of the specific incident solar spectrum (AM1.5 direct). The HCPV/T module's rear is the intended location for the hybrid heat sink that combines jet impingement with an MCHS in a spider-netted structure. This innovative configuration aims to recover the waste heat generated by the absorber components effectively. The receiver and parabolic dish concentrator specifications are presented in Table 1. A Finite Volume Method (FVM) using CFD numerical method and a Monte Carlo Ray-Tracing (MCRT) are coupled together through numerical simulation to overcome the time-dependent complexity of the HCPV/T conversion system in reality, as described in section 3. All HCPV/T layers are characterized in Table 2 concerning their thermophysical and optical properties.

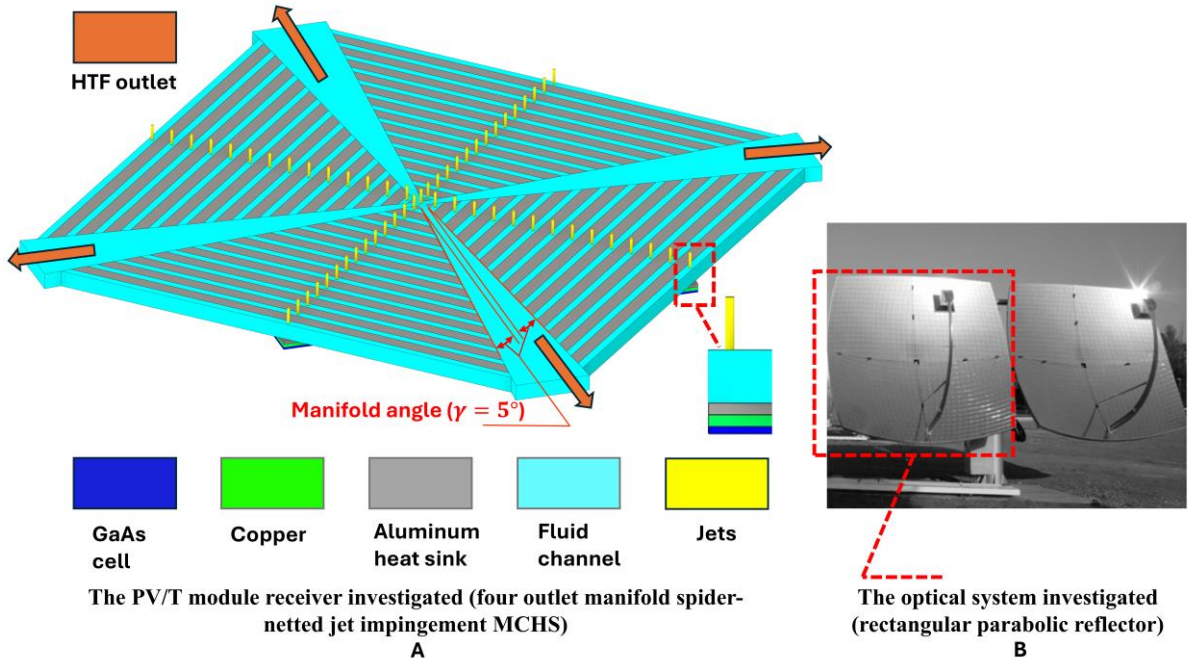

Fig. 1 Visual representation of the suggested model (A) PV/T module receiver investigated and (B) Optical system investigated (Reflector) [32].

Table 1 Specifications for key components of the system.

Components	Parameters	Value
Reflector [32]	Mirror number	1200
	Focal length	2.05 (m)
	Concentrator area	12 (m^2)
	Mirror Area	0.01 (m^2)
Receiver	GaAs solar cell [33]	0. 12 (m) × 0.12 (m) × 0.0006 (m)
	Copper layer	0. 12 (m) × 0.12 (m) × 0.001 (m)
	Heat sink height	0.0055 (m)
	Heat sink design parameter	In Table 6 (Manifold angle)

Table 2 Thermophysical and optical properties of the HCPV/T system.

Component	Density (kg/m^3)	Specific heat (J/kg.k)	Thermal conductivity (W/m.k)	Optical properties
GaAs cell	5320	330	55	[34]
Copper plate	8978	381	387.6	[35]
Aluminum heat sink	2719	871	202.4	[35]

3- Numerical Approaches and Validations

3-1 Hybrid HCPV/T system optical simulation and modelling

The SolTrace optical instrument simulates the parabolic dish's performance by utilizing the efficient and versatile MCRT method, an optical simulation approach used to simulate the Sun's rays and their interactions with different concentrators and receivers. It is used to calculate the concentrated solar heat flux densities. The estimated densities are then introduced into the FLUENT software as thermal boundary conditions for the receiver wall through a user-defined function (UDF). As light travels from the Sun to the end receiver, it encounters many parts of the optical geometry organized in stages according to a global coordinate system. There are two types of interactions: optical (physical interactions with beams) and virtual (helpful in determining flux maps). Elements with their unique characteristics make up one stage. A stage-

related coordinate system characterizes each element. A cumbersome interface results from precisely analyzing the components' shape. A spreadsheet must be utilized to construct all of the optical geometry for each system, which includes:

- Aperture type, surface type, normal direction, optical characteristics, and coordinates are all defined.
- The relationship between the global coordinate system and the coordinate system of each stage is defined [36].

Several steps are involved in the execution of the model in SolTrace:

- Defining sun shape and position.
- Entering the optical properties of optical elements of the system.
- Defining the system geometry in terms of stages and its elements.
- Choosing the number of rays.
- Choosing the DNI for calculations.
- Extracting the solar heat flux intensity.

Based on the Sun's location, this setup necessitates determining the relative positions of all optical components [37]. In the LightTools application, a light source is applied to mimic the sun's rays, and a solid angle of 0.52 degrees is employed to simulate the sun's shape [38], as indicated in Fig. 2. The optical properties of the reflector are assumed to be 0.08, 1, 3 mrad, and one mrad for transmissivity, reflectivity, slope error, and specularity error, respectively [38]. A sunbeam number of 3.0×10^6 is fixed for the conditions of light number independence, as mentioned by S. Lokeswaran, et al. [39]. The AM1.5 direct solar spectrum is subsequently incorporated into the software. A fourth-degree polynomial equation is fitted with the generated solar spectra distribution over the absorber using multiple regression techniques.

In the CFD domain, the solar broadband splits into three wavebands, thermal-band1 [250-447.5 nm], PV-band [447.5-850.3 nm], and thermal-band2 [850.3-4000 nm], in Fluent software, the non-gray DO radiation model is activated. This approach allows for the optical, electrical, and thermal models to be reliably coupled while solving the radiative transfer equation (RTE) and the conservation equations for mass, momentum, and energy, as mentioned in [33, 40]. Using a UDF, the solar spectrum distribution equation imported at the PV laminates' top surface is interpreted as a heat source boundary in each waveband. The polynomial function used in the UDF is defined as :

$$\begin{aligned} F = {} & 1.687e6 + 31{,}657\,X + 62{,}239\,Y + 4.902e8\,X^2 - 1.869e6\,XY - 4.944e8\,Y^2 \\ & + 1.008e6\,X^3 + 1.698e7\,X^2Y + 6.090e6\,XY^2 - 3.391e7\,Y^3 \\ & + 8.459e9\,X^4 + 4.648e8\,X^3Y + 1.584e11\,X^2Y^2 + 1.243e8\,XY^3 \\ & + 9.672e9\,Y^4 \end{aligned} \quad (1)$$

Where the Sun's spectral distribution value (F) is associated with the spatial coordinates (X and Y) of the GaAs solar cell, the fitting results show a relative error of less than 8% compared to the optical simulation results for the Sun's spectral distribution. In the CFD domain, the radiative transfer equation (RTE), as specified [41], is solved by activating the nongray DO model:

$$\nabla.(I_\lambda(\vec{r}.\vec{s})\vec{s}) + \sigma I_\lambda(\vec{r}.\vec{s}) = k_\lambda n^2 I_{b\lambda} + \frac{\beta}{4\pi}\int_0^{4\pi} I_\lambda(\vec{r}.\vec{\hat{s}})\,\varphi(\vec{s}.\vec{\hat{s}})\,d\acute{\Omega} \quad (2)$$

The probability that a ray from one direction, $\vec{s}$, will be scattered into a specific other direction, $\vec{\hat{s}}$, is represented by the scattering phase function φ in the second term of the right side of Eq. (2), which is assumed to be wavelength-independent. In contrast, the emission part is represented by the first term on the same side, where k_λ is the absorption coefficient, and n is the real refractive index. Also, the scattering part on the right side represents the second term, where β is the scattering coefficient. Nevertheless, the extinction coefficient (σ) incorporates the absorption and scattering of light, represented by the second term on the left side. The radiation intensity is denoted by I_λ, and the re-emission term, which is the blackbody emission in the wavelength band per unit solid angle, is denoted by $I_{b\lambda}$, and the solid angle is denoted as

Ώ. The variation of the re-emission term with wavelength is not accounted for in the current model. The extinction coefficient is solely determined by the variation of the absorption coefficient during solar illumination because the scattered spectra of the participating materials are disregarded. Therefore, the RTE equation can be simplified to:

$$\nabla.(I_\lambda(\vec{r}.\vec{s})\vec{s}) + k_\lambda I_\lambda(\vec{r}.\vec{s}) = k_\lambda n^2 I_{b\lambda} \quad (3)$$

For each band (ultraviolet region, visible, or infrared band), the optical equations are solved in numerical calculations in conjunction with a non-gray model in a total number of $N_\phi \times N_\theta$ directions. The RTE equation is computed in $8 \times N_\phi \times N_\theta$ directions for three-dimensional calculations. In addition, pixelations are used to split these control angles. The polar extent N_ϕ and the azimuthal extent N_θ are set at 3, incorporated in the structured mesh. The modelling is conducted with a fixed number of pixelation at 3 and 3 for the azimuthal extent P_θ and the polar extent P_ϕ, respectively [42].

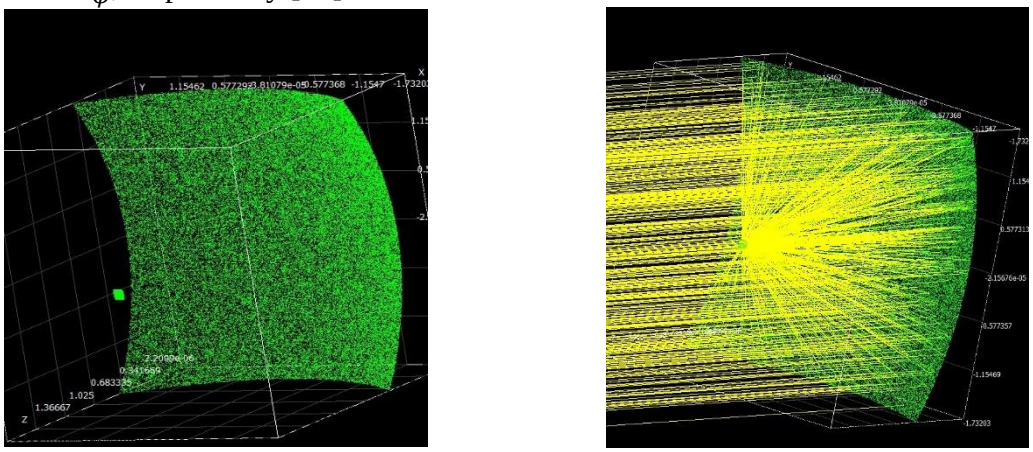

A B

Fig. 2 Visual representation of the parabolic rectangular reflector and receiver in SolTrace software (A) and the ray-tracing model using SolTrace software regarding the solid angle of the Sun (0.52°) (B).

3-2 Hybrid HCPV/T system electric modelling

GaAs cells are among the most desirable options for HCPV/T applications due to their low cost and extensive operating temperature range. It should be noted that cell temperature is not the sole parameter that influences electrical energy efficiency, as indicated by the literature survey listed above. This investigation considers additional variables, including the CR and incident radiation wavelengths (λ) [43].

The cell's dark saturation current, J_{00}, is determined by the following formula:

$$J_{00} = K' T_{pv}^{3/n} \exp\left(\frac{-E_g}{m k_b T_{pv}}\right) \quad (4)$$

Where E_g is the bandgap of the PV cells, T_{pv} is the temperature of the PV cell, and k_b is the Boltzmann constant, and K', m, and n are empirical parameters [44].

The following is the formula for the determination of the short circuit current J_{sc} [45]:

$$J_{sc} = \int_{280}^{\lambda_g} eEQE_\lambda \eta_{opt}(\lambda) F(\lambda) d\lambda \quad (5)$$

Where the electron charge is represented by e, the parabolic dish's optical efficiency ($\eta_{opt}(\lambda)$) is assumed constant at 85% independent of wavelength, λg denotes the wavelength of solar radiation and $F(\lambda)$ denotes the photon flux. The quantum efficiency (EQE_λ) of solar cells is a wavelength-dependent ratio found in references [45, 46] and represents the ratio of carriers gathered by the cell to photons of a particular energy incident on the cell.

Then, using the formula in [45], we can determine the open-circuit voltage, V_{oc}:

$$V_{oc} = \frac{A' k_b T_{pv}}{e} \ln\left(\frac{CRJ_{sc}}{J_{00}} + 1\right) \quad (6)$$

Where the diode factor is represented by A'.

According to Reference [46], the fill factor (FF) (defined as the ratio of the maximum power from the solar cell to the product of J_{sc} and V_{oc}) is defined as:

$$FF = \frac{V_m}{V_{oc}}\left[1 - \frac{\exp\left(\frac{eV_m}{k_b T_{pv}}\right) - 1}{exp\left(\frac{eV_{oc}}{k_b T_{pv}}\right) - 1}\right] \quad (7)$$

Where V_m is the voltage that is derived at the maximum power point of the I-V curve as follows:

$$V_m = B \times V_{oc} \quad (8)$$

Where the value of B is often a number between 0.7 and 0.8.

The reference efficiency of solar cells, which is defined at 25 °C, denoted as η_{ref}, is determined using the formulas given in [45, 46]:

$$\eta_{ref} = \frac{V_{oc} J_{sc} FF}{\int_{280}^{\lambda_g} \eta_{opt}(\lambda) I_\lambda d\lambda} \quad (9)$$

Where I_λ represents the spectral intensity of solar radiation according to the AM1.5 condition. The following equation, which takes the temperature effect into account, calculates the electrical efficiency of solar cells:

$$\eta_{ele} = \frac{P_{ele}}{CR\ A_{cell}\ I_{sun}} = \frac{V_{OC} \times J_{sc} \times FF}{CR\ A_{cell} I_{sun}} = \eta_{ref}(1 - \delta(T_{pv} - T_{ref})) \quad (10)$$

where the gained electric power (P_{ele}) at the PV cell temperature, the reference temperature coefficient (δ), which equals 0.09 % for GaAs cell, and the reference temperature (T_{ref}) are some of the parameters that are involved. The electrical output is determined by combining the actual electrical energy efficiency and the received solar irradiation to accomplish the coupling of electricity and heat [33]. The volumetric heat source term is applied in the part of the GaAs solar cell to simulate the generated electric power with a negative sign, indicating that the electric power is out of the system [43]. Therefore, in the computational domain, the energy source term of the PV layer is activated using the UDF. Table 3 displays the values of the various electrical model parameters and coefficients [43].

Table 3 Definition and value of the various electrical model parameters and coefficients.

Parameters	Definition	Value
K'	Empirical parameter	0.03
m	Empirical parameter	1.15
n	Empirical parameter	0.96
A'	Diode factor	1.1
B	Voltage factor	0.8
A_{cell}	PV area	0.0144 (m^2)

3-3 Hybrid HCPV/T system thermal modelling

With the help of the present modelling technique, this multi-physics system incorporates the thermal model alongside the optical and electric models. The CFD code initializes the RTE and the continuity, momentum, and energy conservation equations in the CFD domain to solve the radiative heat transfer, pressure, velocity, and temperature field in the proposed HCPV/T system. This model is simplified based on the following assumptions:

- A steady-state, incompressible, turbulent flow in three dimensions with one phase is considered.
- Gravitational and other body forces on the body are disregarded [47].
- The thermophysical properties of the fluid and solid domains are assumed to be temperature-independent [20].
- The thermal contact resistances of the solar cells and the MCHS heat absorber are neglected for all layers [48].

- The various refractive indices of the components remain constant [49].
- The channel walls are subjected to a no-slip condition for temperature and velocity [47].
- The cell is considered a volumetric heat source in the model [23].
- The heat loss via the heat sink's rear and the HCPV/T layers' side walls are ignored [50].

The subsequent governing equations can be constructed by implementing the previously indicated assumptions:

Continuity:

$$\nabla.\vec{V} = 0 \tag{11}$$

Momentum:

$$\rho(\vec{V}.\nabla\vec{V}) = -\nabla p + \mu\nabla^2\vec{V} \tag{12}$$

Energy in the fluid domain

$$\rho c_p(\vec{V}.\nabla T) = k\nabla^2 T \tag{13}$$

Energy in GaAs cell domain:

$$k_s\nabla^2 T_s + \nabla q_{rad} + S_h = 0 \tag{14}$$

Energy in other solid domains:

$$k_s\nabla^2 T_s = 0 \tag{15}$$

The radiative term q_{rad}defines the net loss of radiative energy from a control volume, and the volumetric heat source is included in S_h [41]. The HTF absorbs heat and releases it as a thermal output. This study investigates the overall performance of the CPV/T system, including all absorber components. From the thermodynamic viewpoint, the applied concentrated solar spectrum is the energy-in source of the stated domain (control volume). In this way, the thermal energy efficiency of the CPV/T system turns to the relation between the outlet heat gained and the total received energy. Therefore, the thermal energy efficiency of the HCPV/T system can be expressed by the following equation [33]:

$$\eta_{th} = \frac{P_{th}}{CR\ A_{cell} I_{sun}} = \frac{\dot{m}\ c_p(T_{out} - T_{in})}{CR\ A_{cell} I_{sun}} \tag{16}$$

Where the specific heat capacity (c_p), flow rate ($\dot{m}$), the fluid temperature at the inlet and outlet (T_{in} and T_{out}, respectively), and the amount of solar irradiation per unit area (I_{sun}) are some of the parameters that are involved.

However, the power required to circulate the coolant is substantial, and increasing the electrical power output by cooling a PV module is not without its cost. As a result, the final net power calculation of this study has considered the impact of pump power. Therefore, P_{pump}, the power needed to pump the working fluid, is defined as:

$$P_{pump} = \frac{\dot{m}\ \Delta p}{\rho_w} \tag{17}$$

Where Δp represents pressure drop and ρ_w stands for water density. Finally, the investigation of the HCPV/T system's energy performance concludes with the following explanation for net power:

$$P_{net} = P_{ele} - P_{pump} \tag{18}$$

The maximum amount of output energy, or total exergy efficiency ζ_t, can be expressed as [33]:

$$\xi_t = \xi_{ele} + \xi_{th} \tag{19}$$

The values of ζ_{th} and ζ_{ele} are the thermal and electric exergy efficiencies, respectively, and can be defined as follows [51]:

$$\xi_{th} = \eta_{th}\left(1 - \frac{T_a}{T_{out}}\right) \tag{20}$$

Where T_a is the ambient temperature, which is fixed at 300 K.

$$\xi_{ele} = \eta_{ele} \tag{21}$$

3-4 Hybrid HCPV/T system boundary conditions and simulation settings

This study used the ANSYS Fluent code to apply boundary and beginning conditions to the three-dimensional HCPV/T model. The Sun's spectrum, which is evenly distributed as per Eq. 1, falls perpendicularly onto the GaAs cell's top surface and contains the entire spectrum from 280 to 4000 nm. The non-grey DO model is used to separate the solar spectrum into three separate bands of wavelengths, as mentioned in subsection 3.1. The optical properties of all materials are averaged out over each wavelength interval to make them behave as grey media, and the percentage of solar irradiance is added to each band. The top surface of the GaAs material, which is subject to radiation and mixed convection, is considered perpendicular to the incident solar radiation [52]. For the purpose of calculating the external radiation temperature, the formula for the sky temperature, T_{sky}, is as follows [53]:

$$T_{sky} = 0.0552{T_a}^{1.5} \tag{22}$$

A convective heat transfer coefficient is calculated when air passes above a GaAs cell according to [54]:

$$h_w = \begin{cases} 5.7 + 3.8\,V_{wind} \;\; if\; V_{wind} < 5\dfrac{m}{s} \\ 6.47 + {V_{wind}}^{0.78} \; if\; V_{wind} > 5\dfrac{m}{s} \end{cases} \tag{23}$$

Where the local wind speed, denoted as V_{wind}, is fixed at four m/s.The heat loss through the rear of the heat sink and the side walls of the HCPV/T system is disregarded. The fluid domain is subjected to the velocity-inlet boundary condition at the inlet, where the flow rate is adjusted from 0.5 kg/s to 1.3 kg/s, considering the model design, the concentration ratio range, and the solar intensities. The pressure-outlet boundary condition is characterized by a zero-gauge pressure that is applied at the outlet. The fluid domain simulation is conducted using the conventional k-epsilon turbulence model. The electric model can achieve the output power of the GaAs cell by incorporating the source term into the energy equation by using interpreted UDF. With second-order upwind accuracy in the spatial discretization of the governing equations and the application of the global time step approach, the coupled scheme algorithm is used to solve the velocity-pressure couple in the current model. The criterion for convergence during calculation for the continuity, velocity, energy, and DO models are 10^{-3}, 10^{-6}, 10^{-6}, and 10^{-6}, respectively. A 16-core i7-13700 kf processor with 3.4 GHz and 64 MB RAM is used to execute the simulations in CFD Ansys Fluent 2023 R1, with an average of 9 hours to achieve the residual settings requirements.

4- Results and Discussions

4-1 Mesh independent study and validations

The local sizing meshing technique activates the model grid with a maximum skewness rate of 0.56, where hexahedral meshes are employed for different components, as illustrated in Fig. 3 for the reference case. The reliability of the results is ensured by applying the mesh dependence test. As indicated in Table 4, six different grids are used to verify the pressure drop over the heat sink, the outlet temperature, and the output electric power. The 1,822,944 elements grid was ultimately selected for further examination because of this investigation.

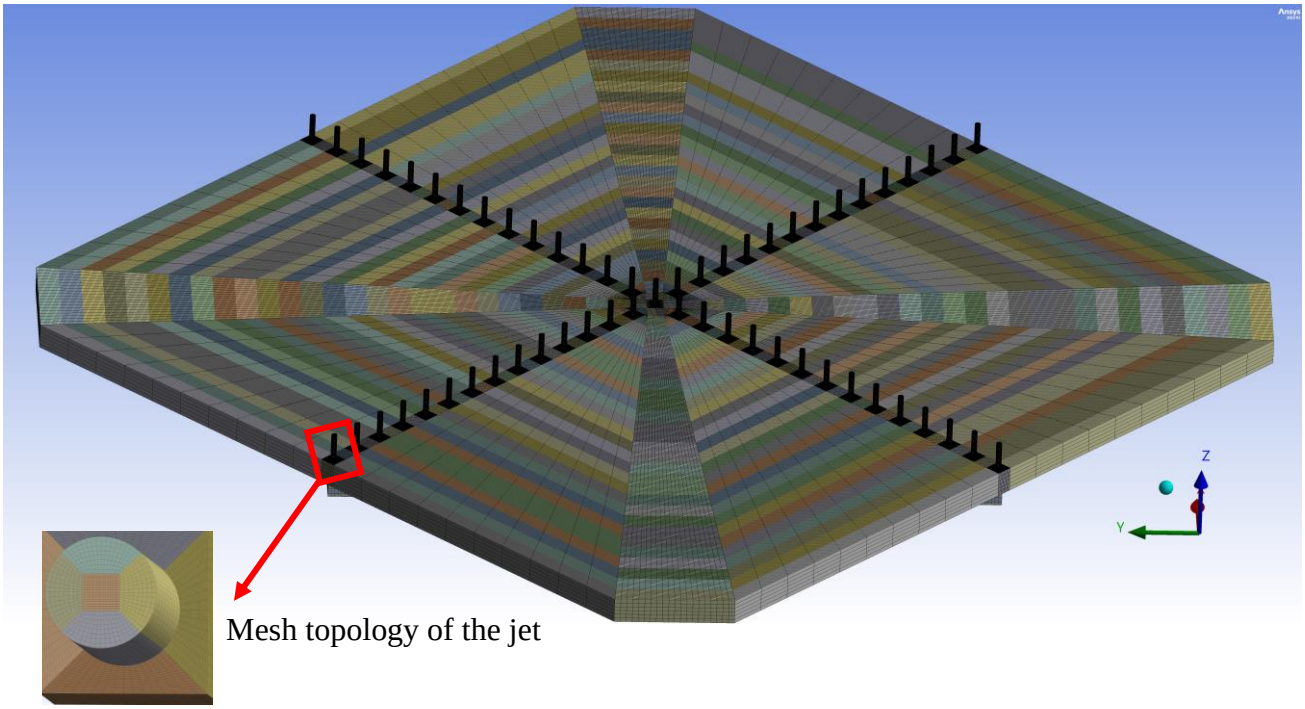

Fig. 3. The grid of the modeled CPV/T system involving the four outlet manifolds at angle 5.

Table 4 Grid independence test for the reference case at DNI of 1000 W/m^2, flow rate of 1.3 kg/s, and inlet temperature of 300 k.

Number of elements	Outlet temperature (K)	Electric power (W)	Pressure drop (kPa)
648,600	301.500	482	94.729
875,864	301.492	519	93.620
1,160,176	301.488	559	92.672
1,303,600	301.486	582	92.264
1,639,984	301.464	626	91.574
1,822,944	301.482	644	91.355

The numerical results are validated by comparing the electrical and thermal energy efficiencies to the experimental measurements taken by Bhattarai et al. [55] from a PV/T module. The parameters used in this validation study are detailed in Table 5. Average errors of 0.67% for electrical energy efficiencies and 2.89% for thermal energy efficiencies are shown in Fig. 4, indicating that the experimental and simulation results are reasonably agreeable.

Table 5 The validation study parameters [55].

Component	Parameter	Value	Unit
Glass cover	Area	2	m^2
	Thickness	0.004	m
	Emissivity	0.88	-
	Absorption coefficient	26	1/m
	Refractive index	1.526	-
PV layer (polycrystalline)	Area of cell	1.607	m^2
	Packing factor	0.804	-
Tube	Outer diameter	0.00952	m
	Thickness	0.0009	m
	Number	10	-
	Length	1.916	m

Operating conditions	Wind speed	1	m/s
	Ambient temperature	303.15	K
	Solar irradiance	800	W/ m^2
	Tilt angle	30	

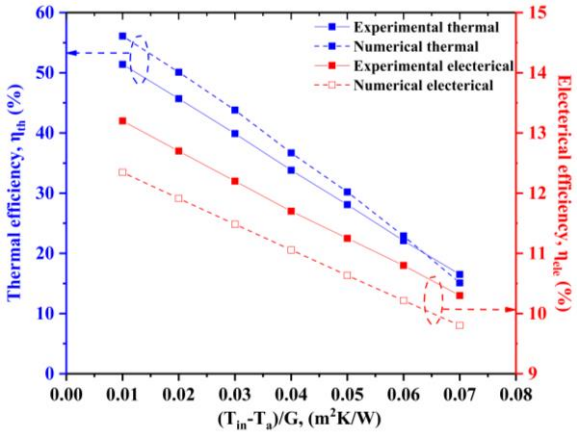

Fig. 4. Validation of the thermal and electrical energy efficiencies of the PV/T module.

Through the utilization of waste heat recovery (WHR) in highly concentrated applications, this section examines the energy and exergy efficiency of the CPV/T system. The effect of the DNI on thermal, energy, and hydraulic performance at different flow rates (0.5 to 1.3 kg/s) is first evaluated using a series of numerical simulations for four outlet manifolds (A). Subsequently, the impact of the manifold angle for all outlets (B) is implemented to improve the overall system performance since the increase in pressure drop and, consequently, pumping power for lower angles results from fluid expansion caused by the alteration in the shape of the central channel in such a way that the resistance in front of the flow becomes higher as the angle decreases, increasing the pumping power required from the jets, as indicated in [30]. All examined parameters are listed in Table 6 and Fig. 5 and will be discussed in the following sections. Note that the optimal case for the design parameter (manifold angle) is illustrated in Fig. 5, defined with black color.

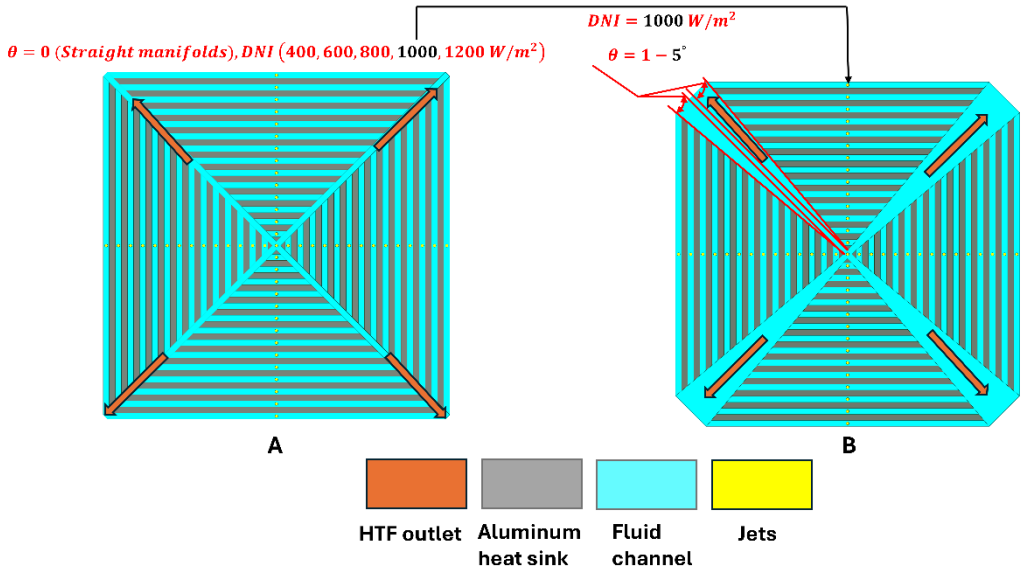

Fig. 5. Visual representation of the investigated parameter of the proposed system

Table 6 Design parameters of the proposed model.

Design parameters	Investigated range	Remarks
(**A**)-DNI	(400-1200 W/m^2)	Applied for solid and fluid width equal 3 mm, a jet diameter which equals 1.5 mm, a jet height which equals 7 mm, and four outlet manifolds.
(**B**)-Manifold angle	(1-5°)	Applied for solid and fluid width equal 3 mm, a jet diameter equals 1.5 mm, a jet height which equals 7 mm, and a DNI of 1000 W/m^2.

4-2 Effect of DNI on the HCPV/T performance

Maintaining the estimated CR fixed at 833 for different DNIs, Fig. 6 (A) and (B) show the mass flow rate versus average PV cell temperature and maximum temperature differential, respectively. The volumetric average temperature of the solar cells increases proportionally when the DNI increases from 400 to 1200 W/m^2, as shown in Fig. 6 (A). As the DNI rises, the solar cell receives more radiation, which causes this trend. Also, the average temperature is inversely proportional to the increase in mass flow rate. As the $\dot{m}$ increases from 0.5 to 1.3 kg/s, the average cell temperature gradually decreases from 84.1 °C to 63.24 °C at 1000 W/m^2. This is because the HCPV/T system dissipates more heat due to the Modified Net Spider Heat Sink's (MNSPHS) increased heat transfer coefficient as the flow rate increases. Additionally, the average temperature drops slowly with an increase in flow rate. The primary cause is insufficient time for the HTF to come into contact with the heated surface of the heat sink [56, 57]. The maximal temperature difference ($\Delta T_{PV} = T_{max} - T_{min}$) is the critical performance assessment criterion for investigating temperature nonuniformity among PV cells in this study [21]. As illustrated in Fig. 6 (B), the maximum temperature difference increases in conjunction with the DNI. The maximum temperature difference exhibits an inverse relationship as the mass flow rate increases from 0.5 to 1.3 kg/s, declining gradually from 103.3 °C to 66.43 °C at 1000 W/m². Notably, the ambient temperature is assumed to have a minimal impact on the performance of the HCPV/T system (CR>10). Thus, the effect of DNI at a constant ambient temperature operation condition is investigated to focus on the impact of DNI separately. Also, the operation temperature of this system reaches about 483 K (maximum temperature of the PV cell at 1200 W/m^2), which is pretty high compared with the ambient temperature (300 k). Thus, in highly concentrated applications, the influence of ambient temperature is minimal compared with other operation parameters.

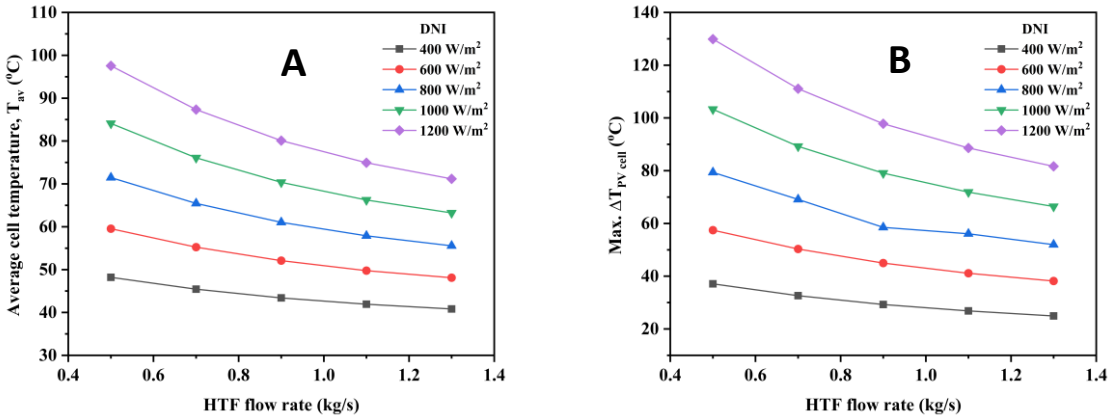

Fig. 6 The average solar cell temperature (A) and maximum temperature difference (B) versus flow rate at different DNI at 0° manifold angle.

Figure 7 (A) and (B) show the electric and thermal power for various DNI and mass flow rates, respectively. Figure 7 (A) illustrates a comparable increase in the electric output of the solar cells as the DNI increases from 400 to 1200 W/m². The relationship between electric power and incoming spectral irradiance intensity is directly proportional, as shown in Eqs. (5 and 10), which is the primary explanation for this trend. In addition, the electric output and the increase in mass flow rate are directly correlated. Specifically, the power generation at 1000 W/m²

increases by 0.451 kW when the flow rate increases from 0.5 to 1.3 kg/s. Eq. (10) describes that both electrical energy efficiency and generated electric power are influenced by incident irradiance and operating temperature. At lower flow rates, generated electric power decreases significantly with increasing DNI due to the sharp rise in PV cell temperature. This temperature increase outweighs the benefits of higher DNI, leading to a dominant negative effect on electric power output. For example, at the lowest flow rate (0.5 kg/s), increasing the DNI from 600 W/m² to 1200 W/m² causes a 0.34 kW drop in electric power. This decline highlights the substantial rise in PV cell temperature under higher DNI and lower flow rate conditions, significantly reducing electric power output. Conversely, as the mass flow rate increases, effective cooling mitigates temperature rise, allowing the higher DNI to enhance PV performance. This results in the highest electric power output observed at the highest flow rate (1.3 kg/s) and the highest DNI (1200 W/m²). The trend underscores the critical impact of flow rate and incident radiation on system performance.

On the other hand, the thermal power increases as the DNI increases, as per Eq. (16), due to the rise in the HTF temperature. In contrast, the thermal power experiences a minor decrease as the flow rate increases. This trend is attributed to the reduction of the amount of thermal energy directly converted from the solar energy received as the electric power increases with the flow rate. Another reason the thermal power drops slightly when the flow rate rises is because the HTF temperature drops a little as well. Specifically, at a DNI of 1200 W/m^2, the maximum thermal power is 12.263 kW at 0.5 kg/s, while at a DNI of 600 W/m^2, the minimum thermal power is 3.649 kW at 1.3 kg/s.

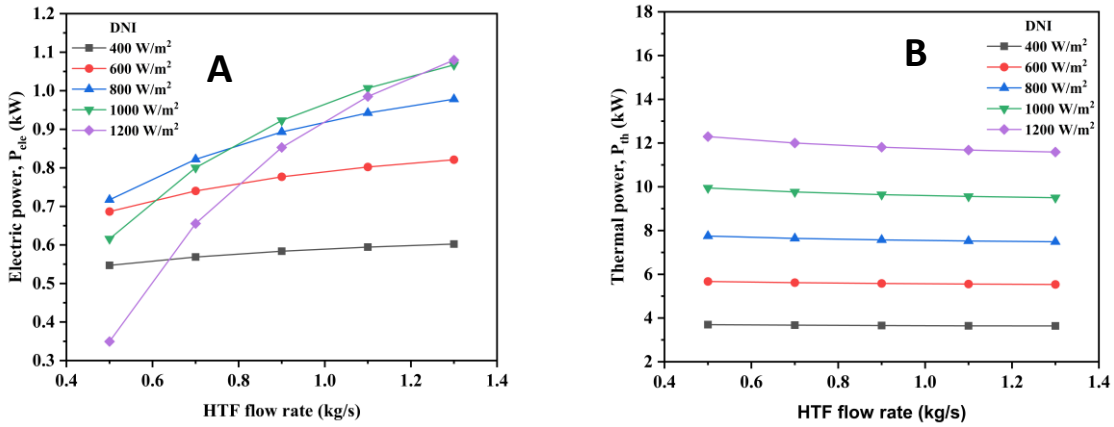

Fig. 7 The electric power (A) and thermal power (B) versus flow rate at different DNI at 0° manifold angle.

In Fig. 8, (A) and (B), the electric and thermal energy efficiencies are illustrated at varying DNI and mass flow rates. The electric energy efficiency of the solar cells decreases when the DNI increases at all flow rates, where the increase of DNI has more influence on the electric energy efficiency of the PV system at low flow rate values. For instance, the electric energy efficiency drops by 8.97% when the DNI rises from 400 to 1200 W/m^2 at the lowest flowrate (0.5 kg/s), while the electric energy efficiency reduces by 5.05% by increasing the DNI from 400 to 1200 W/m² at the highest flowrate (1.3 kg/s). This is because the higher temperature of the cells exceeds the increased radiation that reaches them (refer to Eq. 10). The electric energy efficiency, on the other hand, grows significantly with increasing flow rate at all DNIs, where the increase of flowrate has more influence on the electric energy efficiency of the PV system at high DNI values. For instance, the electric energy efficiency increases by 5.06% and 1.15% at 1200 W/m^2 and 400 W/m^2, respectively, with the flow rate increase from 0.5 to 1.3 kg/s. This is because the convective heat transfer coefficient improves when the flow rate increases, decreasing the cell temperature. In particular, the cooling system that operates on the lowest DNI is the most efficient overall, with electrical energy efficiencies between 11.4% and 12.55% across all coolant flow rates. In contrast, the cooling system with the highest DNI demonstrates the lowest electrical energy efficiency, with 2.43% and 7.49%, at flow rates of 0.5 kg/s and 1.3 kg/s, respectively. Notably, according to the electric energy efficiency

terminology, the electrical energy efficiency attains its lowest value at 0.5 kg/s and 1200 W/m^2 due to the lowest electric power achieved for the above reasons.

The system's thermal energy efficiency followed a similar pattern to its thermal power, contrasting with the electrical energy efficiency in that it declines as the flow rate increases and increases as the DNI increases. The primary reason is that less solar radiation is converted into thermal energy as electrical energy efficiency increases. For instance, the system attains its maximum thermal energy efficiency of 85.4% with the lowest flow rate and highest DNI. The thermal energy efficiency is 75.83% at its lowest point, simultaneously with the highest flow rate and lowest DNI values.

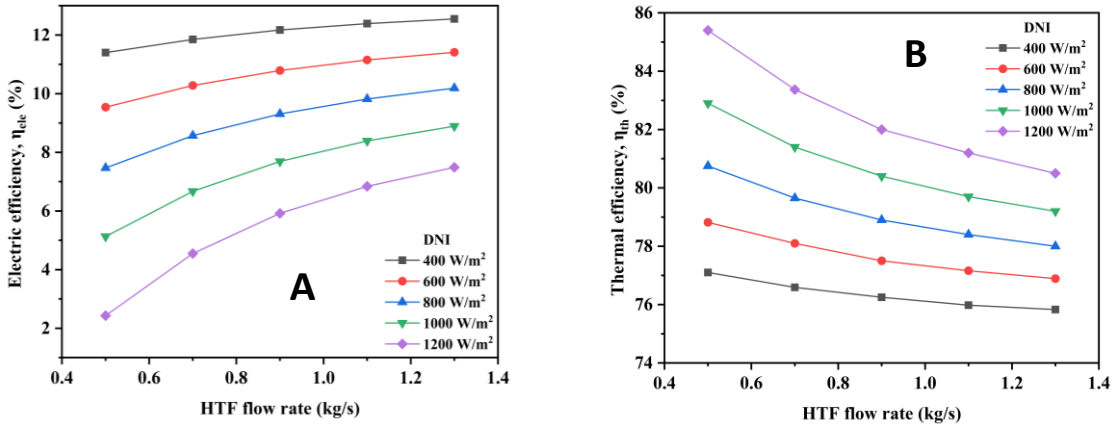

Fig. 8 The electric efficiency (A) and thermal efficiency (B) versus flow rate at different DNI at 0° manifold angle.

Additionally, As illustrated in Fig. 9 (A), (B), and (C), the exergy performance of the proposed system is evaluated by examining the variations in electrical (ζ_{ele}), thermal (ζ_{th}), and total exergy (ζ_{tot}) efficiency across a range of flow rates for all DNI values. Electrical and thermal energy, as well as exergy efficiency, exhibit comparable trends. Notably, the hybrid system's total exergy efficiency is most significantly influenced by electrical efficiency. Remarkably, the exergy content is equal to its energy content for electricity because electrical energy is a form of high-quality energy with 100% conversion potential. So, the electric energy and exergy efficiencies are equal for the same input for electric energy and exergy. At a maximum flow rate of 1.3 kg/s, the DNI of 400 W/m^2 achieves the highest total exergy and electrical efficiencies of 12.99 % and 12.55 %, respectively. Conversely, the maximum thermal exergy efficiency is achieved under distinct circumstances. For instance, a maximum thermal exergy efficiency of 1.64% can be achieved at a minimal flow rate of 0.5 kg/s with a DNI of 1200 W/m^2.

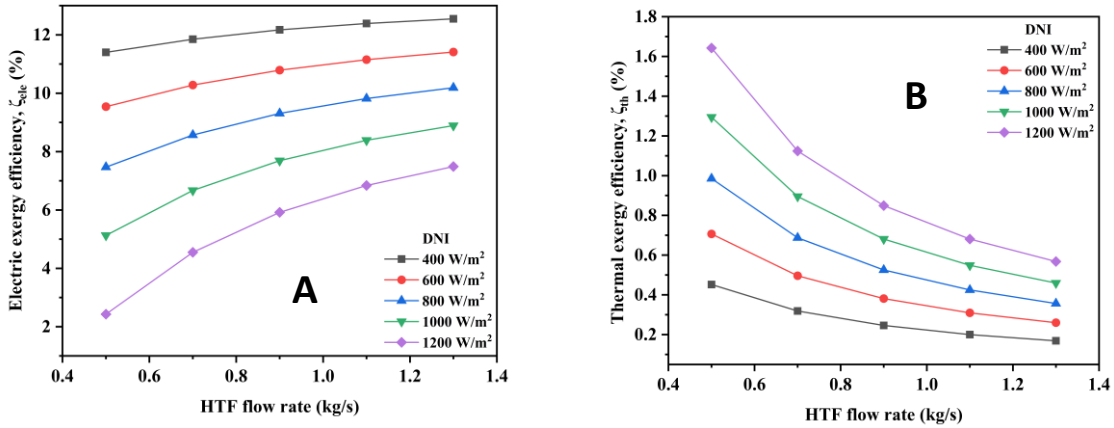

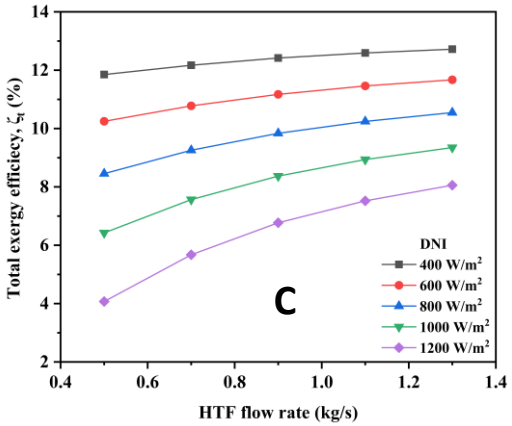

Fig. 9 Variation of (A) electric, (B) thermal, and (C) total exergy efficiencies versus flow rate at different DNI at 0° manifold angle.

The primary factor in selecting the optimal hybrid system design is typically the net power savings. Figure 10 shows that the net obtained electrical power for all DNI values demonstrates an inverse relationship with the flow rate, except for 1000 and 1200 W/m^2 for lower flow rates. The net gained electrical power is mainly determined by the electric power since the pumping power remains constant regardless of the DNI value. For the reasons stated above, it follows that an increase in DNI results in an increase in net gained power proportional to the rise in electric power. According to Eq. (10), electrical efficiency depends solely on the generated electric power, not the net power, leading to differing trends. Unfortunately, this design leads to no net gained power outcomes due to the negative values of the net gained electrical power approximately at all DNI and flow rates due to the excessive pumping power required to operate that system. So, an urgent solution to this concern is a must, and that is what we will discover in the following sections.

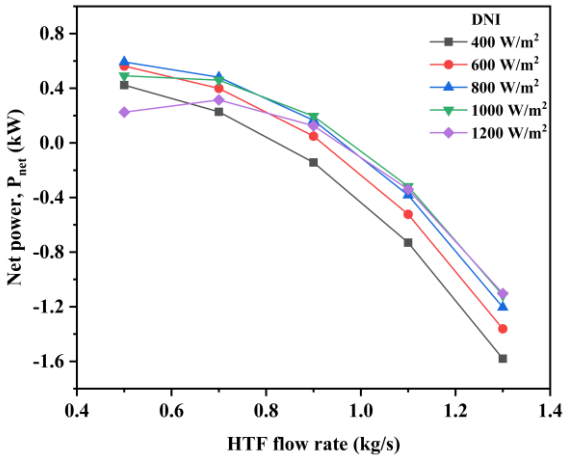

Fig. 10 The net power versus flow rate at different DNI at 0° manifold angle.

.

4-3 Effect of manifold angle (γ) on the HCPV/T performance

Five distinct angles (1, 2, 3, 4, and 5 degrees) are examined to achieve the best design of this four-outlet spider-netted MCHS instead of the zero-degree design employed in the preceding section. Table 7 lists the results of the thermal, energy, and exergy performances for the stated effect of the manifold angle design parameter for various flow rates at a fixed DNI of 1000 W/m^2 and a CR of 833, contrasted with the five-degree angle of the reference case [30].

It can be observed from the results that the maximum temperature difference and volumetric average temperature of the solar cells exhibit a slight variation across all test cases when the manifold angle is varied. In addition, both the average temperature and the maximum temperature difference are inversely proportional to the increase in mass flow rate. As the flow rate increases from 0.5 to 1.3 kg/s, the average cell temperature decreases from 83.8 °C to 62.8 °C.

Instantaneously, the maximal temperature differential decreases from 103 to 65.6 degrees Celsius. This pattern is the result of the MNSPHS's increased heat transfer coefficient, which is facilitated by the high CPV/T system's enhanced heat dissipation. The angle of the manifold is typically directly proportional to the increase of the average temperature and maximum temperature difference. This effect is notably apparent at low flow rates, as thermal resistance is increased due to inadequate mixing. However, the difference becomes negligible with increasing flow rate.

For electric power generated, as the flow rate increases, the trend demonstrates that electrical energy is produced at higher rates across all manifold angles. Specifically, a 0.455 kW increase in power generation occurs when the flow rate goes from 0.5 to 1.3 kg/s at a manifold angle of one degree. Conversely, the electric power output rate drops slightly with different inlet and outlet manifold angles. This phenomenon can be explained by looking at Eq. (10), which demonstrates that the efficiency of photovoltaic cells depends on both the operating temperature and irradiance. Contrarily, heat gained from the system decreases as both the flow rate and manifold angles increase. This effect is primarily because the higher outlet temperature in the former instances directly results from the HTF velocity reduction, making them more efficient. Specifically, at an angle of five degrees, the minimum power is 8.357 kW, and at an angle of one degree, the maximum power is 9.332 kW, with a flow rate of 0.5 kg/s.

Notably, the cooling scheme that operated at the lowest degree angle (angle 1) consistently achieved the highest electrical energy efficiency, which ranged from 5.19% to 8.99%, over the whole range of coolant flow rates. Alternatively, the cooling scheme operating at the higher degree angle 5 achieved the lowest electrical efficiency, with 5.02% and 8.96% values at flow rates of 0.5 and 1.3 kg/s, respectively. Furthermore, unlike electrical efficiency, the thermal energy efficiency of the MSPNHS system decreases as the flow rate rises, following a similar pattern of the system's thermal power. The main reason is that less solar radiation is converted into thermal energy as electrical efficiency increases.

Table 7 also shows how the electrical (ξ_{ele}), thermal (ξ_{th}), and total exergy (ξ_{tot}) efficiency changes for each scenario are studied to evaluate the exergy performance of the proposed system, and this change is observed across different flow rates. Electrical and thermal energy, as well as exergy efficiency, exhibit comparable trends. It should be noted that the overall exergy efficiency of the hybrid system is most affected by electrical energy efficiency. Table 7 shows that at an angle of one degree, the highest electrical energy efficiency is 8.99%, and the total exergy efficiency is 9.39% when the flow rate is 1.3 kg/s. Conversely, the optimum thermal exergy efficiency is achieved under distinct conditions for the same one-degree angle, resulting in a remarkable thermal exergy efficiency of 1.14% at a minimum flow rate of 0.5 kg/s. This differentiation emphasizes the importance of precise operating conditions in achieving optimal results, as it uncovers the crucial effect of flow rate on thermal and electrical exergy efficiencies.

However, the net power gain and the system's efficiency can be significantly diminished by pumping power, a critical metric in hydraulic analysis. The manifold angle influences the hydraulic efficiency considerably, as demonstrated in Table 7. Maximizing hydraulic performance while maintaining overall system efficiency requires careful study of the relationship between manifold angle and flow rate. It is observed that pumping power is increased in all scenarios examined because of the increase in the flow rate as a result of higher pressure drops. Table 7 further demonstrates that the pumping power in the MSPNHS fluid domain decreases as the manifold angle increases. This trend is attributed to the fluid expansion caused by the change in the shape of the central channels, leading to an increase in pumping power for lower angles. Specifically, at a flow rate of 0.5 kg/s, a 98.9% pumping power reduction is observed as the manifold angle increases from 1 to 5 degrees. Accordingly, the pumping power reduction is minimal in a five-degree angle scenario.

Table 7 shows that the net power obtained from these systems is directly proportional to the flow rate. The net power savings peak at 0.9 kg/s and then abruptly decline due to the significant increase in pumping power required by the one-degree angle design. As the manifold angle

Table 7 Investigating the impact of the manifold angle on thermal, energy, and hydraulic characteristics with various flow rates at DNI of 1000 W/m^2.

Effect of manifold angle (°)	Flow rate (kg/s)	T_{av} (°C)	ΔT (°C)	P_{ele} (kw)	P_{th} (kw)	P_{pump} (kw)	P_{net} (kw)	η_{ele} (%)	η_{th} (%)	ξ_{ele} (%)	ξ_{th} (%)	ξ_t (%)
1	0.5	83.82	103.02	0.623	**9.332**	0.025	0.598	5.19	**77.80**	5.19	**1.14**	6.33
	0.7	75.75	88.65	0.810	9.158	0.069	0.740	6.75	76.30	6.75	0.79	7.54
	0.9	69.94	78.35	0.933	9.041	0.147	0.787	7.78	75.37	7.78	0.59	8.38
	1.1	65.79	71.08	1.017	8.955	0.257	0.750	8.48	74.66	8.48	0.48	8.96
	1.3	**62.75**	**65.52**	**1.078**	8.899	0.440	0.638	**8.99**	74.18	**8.99**	0.40	**9.39**
2	0.5	84.02	103.58	0.618	8.965	0.011	0.608	5.15	74.74	5.15	1.05	6.20
	0.7	75.87	88.94	0.807	8.790	0.029	0.778	6.73	73.28	6.73	0.73	7.46
	0.9	70.00	78.48	0.932	8.676	0.061	0.870	7.77	72.33	7.77	0.55	8.32
	1.1	65.83	71.14	1.017	8.610	0.111	0.906	8.47	71.78	8.47	0.45	8.92
	1.3	62.77	65.57	1.078	8.556	0.182	0.896	8.98	71.33	8.98	0.37	9.35
3	0.5	84.25	104.1	0.613	8.641	.0006	0.607	5.11	72.00	5.11	0.98	6.09
	0.7	76.00	89.23	0.804	8.467	0.016	0.788	6.70	70.58	6.70	0.67	7.37
	0.9	70.11	78.62	0.930	8.358	0.033	0.897	7.75	69.67	7.75	0.51	8.26
	1.1	65.88	71.19	1.016	8.295	0.059	0.957	8.47	69.15	8.47	0.41	8.88
	1.3	62.79	65.63	1.077	8.245	0.096	0.981	8.98	68.73	8.98	0.35	9.33
4	0.5	84.51	104.67	0.608	8.436	0.003	0.604	5.07	70.32	5.07	0.93	6.00
	0.7	76.17	89.49	1.801	8.257	0.009	0.792	6.68	68.74	6.68	0.64	7.32
	0.9	70.21	78.73	0.828	8.137	0.019	0.909	7.74	67.83	7.74	0.49	8.23
	1.1	65.95	71.25	1.014	8.085	0.035	0.979	8.46	67.40	8.46	0.39	8.85
	1.3	62.85	65.63	1.076	8.035	0.056	1.021	8.97	66.99	8.97	0.33	9.29
5	0.5	84.79	105.00	0.602	8.357	**0.002**	0.599	5.02	69.67	5.02	0.92	5.94
	0.7	76.36	89.84	0.797	8.175	0.006	0.791	6.65	68.15	6.65	0.63	7.28
	0.9	70.34	78.90	0.926	8.080	0.012	0.914	7.72	67.36	7.72	0.48	8.19
	1.1	66.05	71.30	1.013	8.002	0.021	0.981	8.44	66.71	8.44	0.39	8.83
	1.3	62.92	65.63	1.075	7.955	0.034	**1.073**	8.96	66.32	8.96	0.32	9.28
5 (Reference case)	0.5	96.79	180.78	0.033	8.517	0.008	0.025	0.27	71.00	0.27	0.95	1.22
	0.7	89.36	165.34	0.237	8.381	0.019	0.217	1.98	69.86	1.98	0.66	2.64
	0.9	83.83	154.73	0.381	8.258	0.041	0.339	3.18	68.85	3.18	0.50	3.68
	1.1	79.48	146.43	0.493	8.163	0.073	0.419	4.11	68.10	4.11	0.40	4.51
	1.3	75.99	139.31	0.582	8.082	0.120	0.462	4.85	67.38	4.85	0.33	5.18

increases, this trend becomes less pronounced, as the hybrid system's generated power surpasses the hydraulic power's increase. The most efficient instance among all those tested is the five-degree angle design, which obtained a net power savings of 1.05 kW.

Finally, by comparing the MNSPHS with the other spider-netted microchannel heat sink (MSHS) [30], the modified net spider heat sink eventually outperforms the spider-netted cooling system used in the literature in terms of electric power (84.71%, higher), net output power (135.25%, higher), pumping power (71.67%, lower), and temperature nonuniformity (52.89%, lower) at a manifold angle of 5 degrees and a flow rate of 1.3 kg/s.

5- Conclusion

A microchannel cooling system that is simple, effective, and economical has been developed for high-concentration GaAs solar cells. A shorter fluid channel connecting four outlet manifolds characterizes the newly designed cooling system, in contrast to the longer fluid path in the spider-netted cooling system used in the literature. The results show that high-concentration GaAs solar cells can generate more power and have a higher net output when cooled using systems with a short fluid path, improving thermal characteristics. The primary objective of

this study is to quantify the spider-netted MCHS-jet impingement cooling as an innovative methodology on an HCPV/T system while examining the impact of nonuniform illumination of the heat flux distribution, which is rarely studied. To begin, we can verify the accuracy of the results by comparing the model's numerical solution to the perior experimental data in the literature [55]. Then, the heat sink of the new system is investigated hydraulically, energy-wise, and exergy-wise using a manifold angle design of zero degrees and varying DNI (400, 600, 800, 1000, and 1200 W/m^2). Eventually, varying manifold angles (from one to five degrees) to enhance the overall performance of the HCPV/T system. According to the two parameters examined, the current investigations have produced significant discoveries divided into two categories. These discoveries include:

1- The system achieves its maximum thermal power of 12.263 kW at 1200 W/m² and 0.5 kg/s, while the electric power output rises by 0.451 kW at 1000 W/m² with increased mass flow rate from 0.5 to 1.3 kg/s. Thermal energy efficiency achieves a maximum of 85.4% at the largest DNI and lowest flow rate, while electrical energy efficiency peaks at 12.55% at 400 W/m² and 1.3 kg/s. The total exergy efficiency reaches its peak at 12.99% at 400 W/m² and 1.3 kg/s.
2- The manifold angle slightly affects the maximum temperature difference and average solar cell temperature but significantly improves the hydraulic performance as it increases, achieving net power savings of 1.05 kW at angle 5.

References

1. Qiu, G., Xu, Z., Cai, W.: A novel integrated heating system of solar energy and air source heat pumps and its optimal working condition range in cold regions. Energy Conversion and Management 174, 922-931 (2018).
2. Abo-Zahhad, E.M., Ookawara, S., Radwan, A., El-Shazly, A., El-Kady, M., Esmail, M.F.: Performance, limits, and thermal stress analysis of high concentrator multijunction solar cell under passive cooling conditions. Applied Thermal Engineering 164, 114497 (2020).
3. Kalogirou, S.A., Tripanagnostopoulos, Y.: Hybrid PV/T solar systems for domestic hot water and electricity production. Energy Conversion and Management 47, 3368-3382 (2006).
4. Do, K.H., Kim, T.H., Han, Y.-S., Choi, B.-I., Kim, M.-B.: General correlation of a natural convective heat sink with plate-fins for high concentrating photovoltaic module cooling. Solar Energy 86, 2725-2734 (2012).
5. Sangani, C., Solanki, C.: Experimental evaluation of V-trough (2 suns) PV concentrator system using commercial PV modules. Solar Energy Materials and Solar Cells 91, 453-459 (2007).
6. Lee, S.: Thermal challenges and opportunities in concentrated photovoltaics. In: 2010 12th Electronics Packaging Technology Conference, pp. 608-613. IEEE, (2010).
7. Zhang, H., Chen, H., Liu, H., Huang, J., Guo, X., Li, M.: Design and performance study of a low concentration photovoltaic-thermal module. IJER 42, 2199-2212 (2018).
8. Lee, D.I., Baek, S.W.: Development of a heating system using CPV technology and heat pipes. Environmental Progress & Sustainable Energy 34, 1197-1207 (2015).
9. Jakhar, S., Soni, M.S., Gakkhar, N.: Historical and recent development of concentrating photovoltaic cooling technologies. Renewable and Sustainable Energy Reviews 60, 41-59 (2016).
10. Barrau, J., Omri, M., Chemisana, D., Rosell, J., Ibañez, M., Tadrist, L.: Numerical study of a hybrid jet impingement/micro-channel cooling scheme. Applied Thermal Engineering 33-34, 237-245 (2012).
11. Tuckerman, D.B., Pease, R.F.W.: High-performance heat sinking for VLSI. IEEE Electron device letters 2, 126-129 (1981).

12. Lee, Y.-J., Lee, P.-S., Chou, S.-K.: Enhanced microchannel heat sinks using oblique fins. In: International Electronic Packaging Technical Conference and Exhibition, pp. 253-260. (2009).
13. Micheli, L., Senthilarasu, S., Reddy, K.S., Mallick, T.K.: Applicability of silicon micro-finned heat sinks for 500× concentrating photovoltaics systems. Journal of Materials Science 50, 5378-5388 (2015).
14. Abo-Zahhad, E.M., Ookawara, S., Esmail, M.F.C., El-Shazly, A.H., Elkady, M.F., Radwan, A.: Thermal management of high concentrator solar cell using new designs of stepwise varying width microchannel cooling scheme. Applied Thermal Engineering 172, (2020).
15. Reddy, K.S., Lokeswaran, S., Agarwal, P., Mallick, T.K.: Numerical Investigation of Micro-channel based Active Module Cooling for Solar CPV System. Energy Procedia 54, 400-416 (2014).
16. Kumar, R., Singh, G., Mikielewicz, D.: Numerical study on mitigation of flow maldistribution in parallel microchannel heat sink: channels variable width versus variable height approach. Journal of Electronic Packaging 141, 021009 (2019).
17. Han, J., Guo, G., Pu, C., Zhang, C.: Influence of obstruction's unilateral length on flow and heat transfer performance of micro-channel heat sinks with flow obstructions. Case Studies in Thermal Engineering 50, (2023).
18. Al-Neama, A.F., Kapur, N., Summers, J., Thompson, H.M.: An experimental and numerical investigation of the use of liquid flow in serpentine microchannels for microelectronics cooling. Applied Thermal Engineering 116, 709-723 (2017).
19. Chai, L., Wang, L.: Thermal-hydraulic performance of interrupted microchannel heat sinks with different rib geometries in transverse microchambers. International Journal of Thermal Sciences 127, 201-212 (2018).
20. Hung, T.-C., Yan, W.-M., Li, W.-P.: Analysis of heat transfer characteristics of double-layered microchannel heat sink. International Journal of Heat and Mass Transfer 55, 3090-3099 (2012).
21. Yang, K., Zuo, C.: A novel multi-layer manifold microchannel cooling system for concentrating photovoltaic cells. Energy Conversion and Management 89, 214-221 (2015).
22. Pathak, S.K., Sharma, P.O., Goel, V., Bhattacharyya, S., Aybar, H.Ş., Meyer, J.P.: A detailed review on the performance of photovoltaic/thermal system using various cooling methods. Sustainable Energy Technologies and Assessments 51, (2022).
23. Abo-Zahhad, E.M., Ookawara, S., Radwan, A., El-Shazly, A.H., ElKady, M.F.: Thermal and structure analyses of high concentrator solar cell under confined jet impingement cooling. Energy Conversion and Management 176, 39-54 (2018).
24. Leena, R., Syamkumar, G., Jose Prakash, M.: Experimental and Numerical Analyses of Multiple Jets Impingement Cooling for High-Power Electronics. IEEE Transactions on Components, Packaging and Manufacturing Technology 8, 210-215 (2018).
25. Royne, A., Dey, C., Mills, D.: Cooling of photovoltaic cells under concentrated illumination: a critical review. Solar Energy Materials and Solar Cells 86, 451-483 (2005).
26. Sung, M.K., Mudawar, I.: Experimental and numerical investigation of single-phase heat transfer using a hybrid jet-impingement/micro-channel cooling scheme. International Journal of Heat and Mass Transfer 49, 682-694 (2006).
27. Abo-Zahhad, E.M., Ookawara, S., Radwan, A., El-Shazly, A.H., Elkady, M.F.: Numerical analyses of hybrid jet impingement/microchannel cooling device for thermal management of high concentrator triple-junction solar cell. Applied Energy 253, (2019).
28. Abou-Ziyan, H., Ibrahim, M., Abdel-Hameed, H.: Characteristics enhancement of one-section and two-stepwise microchannels for cooling high-concentration multi-junction photovoltaic cells. Energy Conversion and Management 206, (2020).
29. Torbatinezhad, A., Ranjbar, A.A., Rahimi, M., Gorzin, M.: A new hybrid heatsink design for enhancement of PV cells performance. Energy Reports 8, 6764-6778 (2022).

30. Tan, H., Wu, L., Wang, M., Yang, Z., Du, P.: Heat transfer improvement in microchannel heat sink by topology design and optimization for high heat flux chip cooling. International Journal of Heat and Mass Transfer 129, 681-689 (2019).
31. Chemisana, D., Fernandez, E.F., Riverola, A., Moreno, A.: Fluid-based spectrally selective filters for direct immersed PVT solar systems in building applications. Renewable Energy 123, 263-272 (2018).
32. Chayet, H., Lozovsky, I., Kost, O., Loeckenhoff, R., Rasch, K.D.: High efficiency, low cost parabolic dish system for cogeneration of electricity and heat. In: AIP Conference Proceedings, pp. 175-178. American Institute of Physics, (2010).
33. Abd El-Samie, M.M., Li, W., Xu, C., Ju, X.: Influence of thermal and optical criteria of spectral fluid filters for hybrid concentrated photovoltaic/thermal systems. International Journal of Heat and Mass Transfer 174, (2021).
34. Adachi, S.: Properties of aluminium gallium arsenide. IET (1993).
35. Axelevitch, A., Gorenstein, B., Golan, G.: Investigation of Optical Transmission in Thin Metal Films. Physics Procedia 32, 1-13 (2012).
36. Nepveu, F., Ferrière, A., Ulmer, S., Rodriguez, B.: Optical simulation of a 10 kWel dish/stirling unit using ray-tracing code SOLTRACE. (2008).
37. Garcia, P., Ferriere, A., Bezian, J.-J.: Codes for solar flux calculation dedicated to central receiver system applications: A comparative review. Solar Energy 82, 189-197 (2008).
38. Chayet, H., Lozovsky, I., Kost, O., Loeckenhoff, R., Rasch, K.-D., Bett, A.W., McConnell, R.D., Sala, G., Dimroth, F.: High Efficiency, Low Cost Parabolic Dish System for Cogeneration of Electricity and Heat. pp. 175-178 (2010).
39. Lokeswaran, S., Mallick, T.K., Reddy, K.S.: Design and analysis of dense array CPV receiver for square parabolic dish system with CPC array as secondary concentrator. Solar Energy 199, 782-795 (2020).
40. Adam, S.A., Ju, X., Lin, J., Xu, C., Abdelmagid, T.I., Ahmed, I.A., Abd El-Samie, M.M.: Influence of material properties of liquid absorption filters for concentrated photovoltaic/thermal hybrid systems. Applied Thermal Engineering 123639 (2024).
41. Modest, M.F., Mazumder, S.: Radiative heat transfer. Academic press (2021).
42. Ju, X., Abd El-Samie, M.M., Xu, C., Yu, H., Pan, X., Yang, Y.: A fully coupled numerical simulation of a hybrid concentrated photovoltaic/thermal system that employs a therminol VP-1 based nanofluid as a spectral beam filter. Applied Energy 264, (2020).
43. Li, W., Abd El-Samie, M.M., Zhao, S., Lin, J., Ju, X., Xu, C.: Division methods and selection principles for the ideal optical window of spectral beam splitting photovoltaic/thermal systems. Energy Conversion and Management 247, (2021).
44. Hassani, S., Taylor, R.A., Mekhilef, S., Saidur, R.: A cascade nanofluid-based PV/T system with optimized optical and thermal properties. Energy 112, 963-975 (2016).
45. Otanicar, T., Taylor, R., Telang, C.: Photovoltaic/thermal system performance utilizing thin film and nanoparticle dispersion based optical filters. Journal of Renewable and Sustainable Energy 5, (2013).
46. Fan, J.C.: Theoretical temperature dependence of solar cell parameters. Solar cells 17, 309-315 (1986).
47. Tran, N., Chang, Y.-J., Wang, C.-C.: Optimization of thermal performance of multi-nozzle trapezoidal microchannel heat sinks by using nanofluids of Al2O3 and TiO2. International Journal of Heat and Mass Transfer 117, 787-798 (2018).
48. Radwan, A., Ahmed, M.: Thermal management of concentrator photovoltaic systems using microchannel heat sink with nanofluids. Sol. Energy 171, 229-246 (2018).
49. Jing, D., Hu, Y., Liu, M., Wei, J., Guo, L.: Preparation of highly dispersed nanofluid and CFD study of its utilization in a concentrating PV/T system. Sol. Energy 112, 30-40 (2015).
50. Radwan, A., Ookawara, S., Ahmed, M.: Analysis and simulation of concentrating photovoltaic systems with a microchannel heat sink. Sol. Energy 136, 35-48 (2016).

51. Abd El-Samie, M.M., Ju, X., Xu, C., Du, X., Zhu, Q.: Numerical study of a photovoltaic/thermal hybrid system with nanofluid based spectral beam filters. Energy Conversion and Management 174, 686-704 (2018).
52. Maadi, S.R., Khatibi, M., Ebrahimnia-Bajestan, E., Wood, D.: Coupled thermal-optical numerical modeling of PV/T module – Combining CFD approach and two-band radiation DO model. Energy Conversion and Management 198, (2019).
53. Swinbank, W.C.: Long-wave radiation from clear skies. Quarterly Journal of the Royal Meteorological Society 89, 339-348 (1963).
54. Maadi, S.R., Kolahan, A., Passandideh-Fard, M., Sardarabadi, M., Moloudi, R.: Characterization of PVT systems equipped with nanofluids-based collector from entropy generation. Energy Conversion and Management 150, 515-531 (2017).
55. Bhattarai, S., Oh, J.-H., Euh, S.-H., Krishna Kafle, G., Hyun Kim, D.: Simulation and model validation of sheet and tube type photovoltaic thermal solar system and conventional solar collecting system in transient states. Solar Energy Materials and Solar Cells 103, 184-193 (2012).
56. Bahaidarah, H.M.S.: Experimental performance evaluation and modeling of jet impingement cooling for thermal management of photovoltaics. Solar Energy 135, 605-617 (2016).
57. Baloch, A.A.B., Bahaidarah, H.M.S., Gandhidasan, P., Al-Sulaiman, F.A.: Experimental and numerical performance analysis of a converging channel heat exchanger for PV cooling. Energy Conversion and Management 103, 14-27 (2015).